Modeling Superheat Removal during Continuous Casting of Steel Slabs

X. HUANG, B.G. THOMAS, and F.M. NAJJAR

To investigate superheat dissipation in a continuous slab casting machine, mathematical models have been developed to compute fluid flow velocities, temperature distribution within the liquid pool, heat transfer to the inside of the solidifying shell, and its effect on growth of the shell. Three-dimensional (3-D) velocity and heat-transfer predictions compare reasonably with previous experimental measurements and two-dimensional (2-D) calculations. The results indicate that the maximum heat input to the shell occurs near the impingement point on the narrow face and confirm that most of the superheat is dissipated in or just below the mold. Superheat temperature and casting speed have the most important and direct influence on heat flux. The effects of other variables, including mold width, nozzle jet angle, and submergence depth, are also investigated. Calculated heat flux profiles are then input to a one-dimensional (1-D) solidification model to calculate growth of the shell. Shell thickness profiles down the wide and narrow faces are compared with the predictions of conventional heat conduction models and available measurements.

I. INTRODUCTION

STEEL is poured into the mold at a temperature above the liquidus. The sensible heat contained in the liquid steel represented by this temperature difference is known as the superheat. The average rate of removal of superheat, Q_{sh}, (kW) can be calculated from*

*Symbols are defined in Table I.

$$Q_{sh} = (T_0 - T_{liq})\, \rho C_p V_z W N \qquad [1]$$

The temperature difference between T_0 and T_{liq} is referred to as the superheat temperature, ΔT_s, and should not be confused with the superheat itself. Superheat is important because

(1) it must be removed before the steel can solidify;
(2) it has a great effect on the solidified microstructure; and
(3) it affects the formation of defects, such as breakouts, oscillation marks, and cracks, through its influence on the formation of the growing shell.

The superheat can be advected to the solidifying steel shell while in the mold and conducted through the shell to the copper mold walls, and it can travel below the mold region and dissipate lower in the caster. Assuming 60 pct of the superheat in Eq. [1] is removed by the mold, approximate calculations show that this superheat removal rate (501 kW) represents about 20 pct of the total heat extracted by the mold (2481 kW). These calculations are given in Appendix I for typical slab casting conditions (case B in Table I).[1]

In a slab caster, the steel jet usually impinges first on the solidifying shell near the narrow face. This produces a local maximum in superheat extraction at this location, so a disproportionately large amount of the superheat is delivered to the narrow face.[1] In addition, the rate of heat extraction from the solidified shell by the narrow faces of the mold is usually less than from the wide faces[2] because of poorer contact and larger interfacial gaps. Moreover, Appendix I shows that the total superheat extraction rate (835 kW) is more than twice the power needed to continuously form a uniform, 10-mm-thick shell on the narrow faces (347 kW). These numbers indicate that the manner of superheat dissipation in the mold is very important. If too much superheat is delivered to the narrow faces, then shell growth there may significantly slow down or even reverse locally. This is likely to increase the incidence of breakouts near the narrow faces and could have an important effect on other quality problems as well.

Superheat also has an important effect on surface defect formation. By increasing heat input locally to the inside of the solidifying shell, it can slow down or even stop shell growth and produce local hot spots on the outer surface of the shell.[3] Upon exiting the mold, this hotter and thinner shell is more susceptible to deformation, bulging, and crack formation. Equally important is the temperature of the steel near the meniscus. If most of the superheat is removed before reaching the meniscus, the temperature of the melt may be too low during the critical first stage of solidification. This would allow both freezing of the meniscus and excessive solidification of a thick slag rim. This could lead to quality problems, such as deeper oscillation marks, which later initiate transverse cracks.

Finally, superheat has an important influence on the microstructure and internal quality.[4] Crystals that nucleate in the mold can survive to grow into equiaxed grains only if the liquid alloy surrounding them is colder than their melting temperature. Their survival is more likely at low superheat, when the crystals can sink or be carried down through the mold to the cooler liquid pool below.

X. HUANG, Research Associate, B.G. THOMAS, Associate Professor, and F.M. NAJJAR, Graduate Student, are with the Department of Mechanical and Industrial Engineering, University of Illinois, Urbana, IL, 61801.

Manuscript submitted September 10, 1990.

Table I. Simulation Conditions and Nomenclature

Symbol	Variable	*A* (Standard)	*B*[1]*
C_p	specific heat (liquid steel)	680 J kg^{-1} K^{-1}	720 J kg^{-1} K^{-1}
C_{ps}	specific heat (solid steel)	690 J kg^{-1} K^{-1}	
E	wall roughness constant	0.8	
Fr*	modified Froude number (inlet), $(v_{x0}^2\, g^{-1}\, L_w^{-1}\, \beta^{-1}\, \Delta T_s^{-1})$	770	713
f_s	solid fraction		
g	gravitational acceleration	9.8 m s^{-2}	
H	enthalpy (solid steel) (J kg^{-1})		
ΔH_L	latent heat of fusion	272,000 J kg^{-1}	
h	heat-transfer coefficient (top surface)	40 W m^{-2} K^{-1}	
K	turbulent kinetic energy (inlet and initial)	0.0502 m^2 s^{-2}	
k_{eff}	effective thermal conductivity (liquid steel)	see Eq. [3]	
k_0	laminar thermal conductivity	26 W m^{-1} K^{-1}	
k_s	thermal conductivity (solid steel)	29.3 Wm^{-1} K^{-1}	
	inlet dimensions (nozzle)		
L_h	height	38 mm	45 mm
L_w	width	60 mm	
L_m	working mold length	0.6 m	0.6 m
	total mold length	0.7 m	
L_n	nozzle submergence depth	0.265 m	0.100 m
N	slab mold thickness (across narrow face)	0.22 m	
Pr_0	laminar Prandtl number $(C_p \mu_0 k_0^{-1})$	0.1	
Pr_t	turbulent Prandtl number	0.9	
p	static pressure (relative to outlet plane)		
q	heat extraction function to mold (kW m^{-2})		Q_M in Reference 1, Fig. 19
q_p, q_{sh}	calculated heat flux (from liquid to shell)	see Fig. 5(a)	Fig. 5(b)
Re	Reynolds number		
	inlet $(v_{x0} \sqrt{L_h L_w}\, \rho \mu_0^{-1})$	65,000	69,300
	outlet $(V_z \sqrt{N\, W}\, \rho \mu_0^{-1})$	11,400	16,100
T	temperature (°C)		
T_{liq}	liquidus temperature (at wall)	1525 °C (2777 °F)	1531 °C
T_0	casting temperature (at inlet)	1550 °C (2822 °F)	1558 °C
T_{sol}	solidus temperature	1518 °C	
T_∞	ambient temperature (above top surface of powder layer)	27 °C (81 °F)	
ΔT_s	superheat temperature $(T_0 - T_{\text{liq}})$	25 °C (45 °F)	27 °C
t	time below meniscus (s)		
Δt	time step size	0.003 s	
V_z	casting speed	0.0167 m s^{-1} (39 in./min^{-1})	0.0267 m s^{-1} (63 in./min^{-1})
v_x	velocity component in x direction	see Eq. [2]	
v_{x0}	normal velocity through inlet (peak)	1.062 m s^{-1}	
v_y	velocity component in y direction	see Eq. [2]	
v_{y0}	horizontal velocity through inlet plane	0.0 m s^{-1}	
v_z	velocity component in z direction	see Eq. [2]	
v_{z0}	downward velocity through inlet	0.471 m s^{-1}	
W	slab mold width	1.32 m (52 in.)	1.05 m
x	coordinate (mold width direction)	see Fig. 1	
Δx	node size	1.0 mm	
y	coordinate (mold thickness direction)	see Fig. 1	
y_n	distance of near-wall node from wall	7 to 9 mm	
Z	caster length simulated	3.00 m	
z	coordinate (casting direction)	see Fig. 1	
α	jet angle (at inlet)	24 deg down	20 deg down
α_0	nominal nozzle angle (at inlet)	15 deg down	12 deg down
β	thermal expansion coefficient (liquid steel)	1.0×10^{-4} $°C^{-1}$	
ε	dissipation rate (inlet and initial)	0.457 m^2 s^{-3}	
κ	Von Karmen constant	0.4	
μ_{eff}	effective viscosity (liquid steel at inlet)	3.490 kg m^{-1} s^{-1}	
μ_0	laminar (molecular) viscosity	0.00555 kg m^{-1} s^{-1}	
μ_t	turbulent viscosity (liquid steel at inlet)	3.484 kg m^{-1} s^{-1}	
ρ	density (liquid steel)	7020 kg m^{-3}	6968 kg m^{-3}
ρ_s	density (solid steel)	8000 kg m^{-3}	

*Unlisted values are the same as case A.

When sufficient numbers of crystals survive their journey through the mold and are deposited ahead of the growing columnar grains lower in the strand, a larger central equiaxed zone results.

Superheat is one of the few casting variables that has been conclusively linked to centerline macrosegregation.[5,6] A high superheat exacerbates this problem, which has a corresponding detrimental effect on mechanical properties.[5,6] At high superheat, nucleation is not possible in the hot bulk of the liquid. In addition, any nuclei convected into the hotter liquid away from the walls are likely to remelt before reaching the cooler regions deeper in the caster. Thus, fewer nuclei remain to initiate the central equiaxed zone, and a large columnar zone results.[4,6] The success of mold electromagnetic stirring to improve microstructure has been attributed, in large part, to its effect on superheat removal and movement of these nuclei.[7]

In light of its importance, the present project was undertaken to investigate how superheat is dissipated in the continuous slab casting process under various conditions and to determine how this superheat affects shell growth. In this work, mathematical models are employed to calculate the velocity and corresponding temperature fields within the molten steel. Heat flux profiles down the mold walls are then extracted and used in a second model to predict shell growth and temperature distribution within the shell as it moves through the mold.

The effects of important casting variables on superheat removal are investigated, including steel grade, superheat temperature, casting speed, mold width, nozzle submergence depth, and nozzle port geometry, through its effect on jet angle and profile leaving the nozzle.

II. PREVIOUS MODELS

The importance of superheat removal to the continuous casting process is well known. However, most previous mathematical heat flow/solidification models of the process oversimplify the important effects of fluid flow on superheat distribution.[8,9,10] In these models, the heat transferred by turbulent fluid convection is approximated by simple heat conduction, where the thermal conductivity of the liquid phase is usually raised by a constant factor of about 7.

Mathematical models have recently been applied to calculate fluid flow in the continuous slab casting mold.[3,11–15] However, only a few models have been applied to better understand superheat dissipation in continuous casting molds. Nakato *et al.*[1] used heat convection measurements for water jets on plates to predict heat flux to the narrow face and compared these with experimental measurements. Recently, Flint[3] used a finite difference model (PHOENICS) to solve the coupled three-dimensional (3-D) equations which govern turbulent fluid and energy transport, including the effects of latent heat. This model was used to calculate both the flow pattern and temperature contours, including the solidification and withdrawal of the strand, and predicted significant thinning of the solid steel shell on the narrow face and adjacent edges of the wide face.

III. FLUID AND HEAT FLOW MODEL IN LIQUID

To further understand superheat removal in continuous slab casting, a numerical model based on the finite-volume method has been developed to calculate the fluid flow and temperature distribution within the molten steel pool inside the shell in the mold region of a continuous slab casting machine. Figure 1 shows the 60 × 34 × 16 grid of nodes used to model the liquid pool in the present work. Twofold symmetry is assumed so only one quarter of the mold is modeled. The heat-transfer model calculates temperatures in this domain by solving a 3-D energy conservation equation:

$$\rho C_p\left(v_x\frac{\partial T}{\partial x}+v_y\frac{\partial T}{\partial y}+v_z\frac{\partial T}{\partial z}\right)=\frac{\partial}{\partial x}\left(k_{\text{eff}}\frac{\partial T}{\partial x}\right)+\frac{\partial}{\partial y}\left(k_{\text{eff}}\frac{\partial T}{\partial y}\right)+\frac{\partial}{\partial z}\left(k_{\text{eff}}\frac{\partial T}{\partial z}\right) \quad [2]$$

A 3-D fluid flow model was used to calculate the velocities v_x, v_y, and v_z needed in the above equation, by solving the equations given in Appendix II, assuming steady-state, incompressible, turbulent, single-phase flow conditions. Further discussion of this work and comparison of the flow results with water model observations and measurements is given elsewhere.[15,16,17]

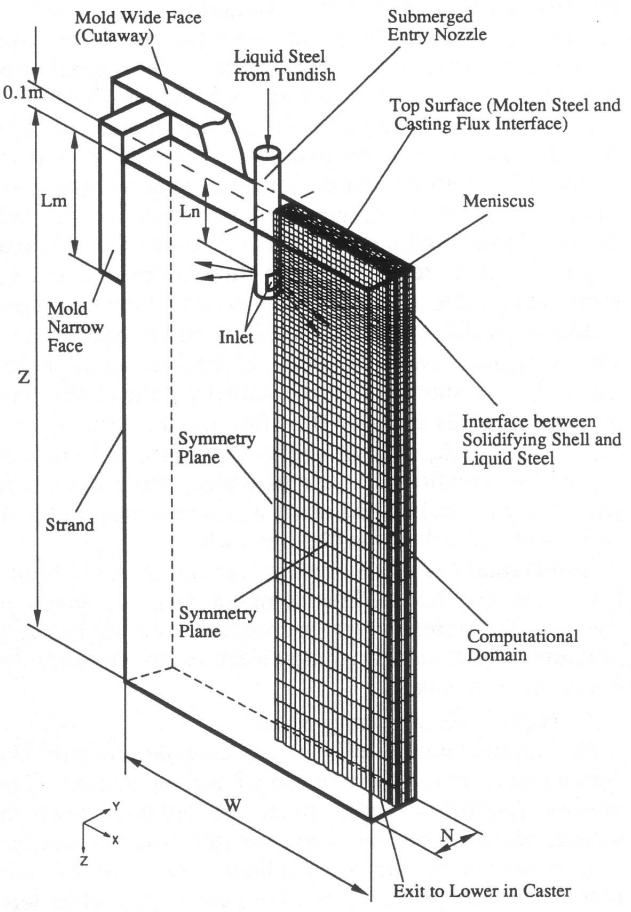

Fig. 1—Simulation domain and typical mesh used in the 3-D fluid flow and heat-transfer model.

The Reynolds number in the caster, based on the hydraulic diameter, (Table I) always exceeds 10,000, even far below the mold. This indicates that the flow is highly turbulent everywhere. Thus, the K-ε turbulence model is used in calculating velocities.[18] In addition, conductive heat transfer is enhanced greatly by turbulent eddy motion, so the effective thermal conductivity, k_{eff}, consists of two components:

$$k_{\text{eff}} = k_0 + \frac{C_p \mu_t}{\text{Pr}_t} \quad [3]$$

It is important to note that the effective conductivity depends greatly on the turbulence parameters through the calculated turbulent viscosity, μ_t, defined in Appendix II, and the turbulent Prandtl number, Pr_t,[14] which is set to the standard value of 0.9 in the present work.[19]

Single-phase flow was assumed, so effects such as those from argon gas bubble injection are not considered. In most runs, the effect of buoyancy forces (from composition or temperature-induced density differences) on the velocity fields was also neglected. This allowed the energy equation to be uncoupled from the other equations.

A. *Boundary Conditions*

1. *Inlet*

The mold cavity is fed by a bifurcated, submerged entry nozzle, which has an important influence on the flow pattern. To account for this, velocity components, v_{x0}, v_{y0}, and v_{z0}, and turbulence parameters, K and ε, are fixed at the inlet plane to the mold cavity. The normal component, v_{x0}, controls the casting speed and is given either a constant value or a parabolic profile, increasing from 0 at the top of the inlet plane to the peak value at the bottom. The vertical component, v_{z0}, which controls the initial jet angle is given the same way as v_{x0}, and the horizontal component v_{y0}, which controls the spread angle, is set to zero. The inlet dimensions, L_h and L_w, correspond to the area of the nozzle port where steel flows outward. Because recirculating flow enters back into the top of typical oversized ports of nozzles used in service,[15] L_h is shorter than the actual height of the port. All of the values defining flow through the inlet, v_{x0}, v_{y0}, and v_{z0}, K, ε, L_h, and L_w are given in Table I and correspond to conditions at the exit plane from the nozzle port. They are calculated using a separate model of fluid flow in the nozzle, described elsewhere.[15,16,20]

Temperature across the inlet plane (nozzle exit) is simply fixed to the casting temperature, T_0, given in Table I. This temperature corresponds to a tundish temperature, because the temperature drop through the nozzle is very small.[21]

2. *Outlet and symmetry planes*

For computational efficiency, calculations are performed only in the top portion of the liquid pool. This creates an artificial outlet plane, at length Z down the strand, where flow leaves the domain. Across this bottom outlet plane, normal gradients ($\partial/\partial z$) of all variables, including T, v_x, v_y, v_z, K, ε, and p, are set to zero. The same boundary conditions are used for each node on a symmetry centerplane, except that the velocity component normal to the symmetry plane is set to zero.

3. *Top surface*

The top surface is treated the same as a symmetry plane, except for temperature. Calculations were made to estimate heat conduction through the molten flux and powder layers and radiation to ambient. To account for this heat loss, an equivalent thermal convection boundary condition is applied to the top surface, using the heat-transfer coefficient, h, and ambient temperature, T_∞, given in Table I. The small variations in the liquid level due to motion of the free surface are neglected.

4. *Mold wall*

To avoid the computational difficulties associated with modeling latent heat evolution at the solidification front, fluid flow is modeled up to, but not including, the mushy zone. The boundaries of the mesh along the narrow and wide face walls then correspond to the dendrite tips forming the outer limit of the mushy zone. Consequently, a fixed temperature, nominally equal to the liquidus, T_{liq}, is imposed along the narrow and wide face mold walls, which should behave like a rough solid wall.

To account for the steep gradients that exist near the walls, empirical "wall law" functions, given in Appendix III, are employed to define the tangential velocities, K, ε, and T, at the near-wall grid nodes. The thermal wall function was found to be very important, particularly for achieving an accurate heat balance. It was used to calculate the heat flux due to superheat dissipation, q_{sh}, which is presented graphically in Section IV and is input to other models of the solidifying steel shell (described in Section VII).

This approach differs from other recent models, which couple the fluid flow and solidification calculations. The latter models use a function (based on flow through porous media) to radically reduce velocity and turbulence levels within the mushy zone.[3] By separating the fluid flow and solidification calculations, the present approach reduces the complexity of the heat conduction and solidification model of the solid shell. Results from this model can also be easily coupled with other thermal stress and shrinkage models that incorporate heat flow across the growing gap.[22]

B. *Solution Method*

Owing to the regular rectangular geometry of the mold, a computer code based on finite difference calculations, MUPFAHT,[23] has been chosen for this complex problem. The steady-state (elliptic) system of differential equations and boundary conditions is discretized into finite difference equations using a staggered grid and seven-point stencil of control volumes. To aid convergence, an upwinding scheme is employed for the advection terms in domains with high cell Reynold's number.[24] In addition, the source terms are linearized to increase diagonal dominance of the coefficient matrix.[24] The equations are solved with the semiimplicit method of pressure-linked equations algorithm, whose alternating-direction, semi-implicit iteration scheme consists of three successive tri-diagonal matrix algorithm solutions (one for each coordinate direction) followed by a pressure-velocity modification to satisfy the mass conservation Eq. [A2.1].[24]

Obtaining reasonably converged velocity and turbulence fields for this problem is difficult, owing to the high degree of recirculation. The current strategy employed is successive iteration using an underrelaxation factor of 0.2 or 0.3 until the maximum relative residual error and maximum relative error between successive solutions falls below 0.1 pct. Over 2500 iterations are required to achieve this, starting from an initial guess of zero velocity, which takes about 30 CPU hours on a Silicon Graphics 4D/25 workstation. For subsequent processing conditions, convergence from a previously obtained solution is much faster. Solving the energy equation is much easier, because it needs fewer iterations with just one unknown and requires only 2 hours of CPU time. However, the temperature solution is very sensitive to the convergence of the velocity and turbulence fields, so the stringent convergence requirement of 0.1 pct must be satisfied when velocity solutions are used in subsequent heat-transfer calculations.

IV. MODEL RESULTS AND DISCUSSION

Model calculations of velocity, temperature, and heat flux are now presented and compared with available measurements. All of the results were obtained by running the 3-D finite difference fluid flow and heat flow models under standard casting conditions, designated as case A in Table I, except where indicated otherwise. The post processor FIPOST of the commercial finite element program FIDAP[18] was used to visualize and plot the results.

A. *Velocity*

Figure 2 presents typical 3-D model results for velocity, temperature, and heat flux (case A). The first two frames viewing the centerline section show how flow leaves the nozzle as a strong hot jet, which carries heat with it across the mold to impinge upon the narrow face. The flow then splits vertically to create upper and lower recirculation regions. Figure 3 reveals the interior flow pattern with transverse sections taken at seven locations down the mold. These show how the initial jet expands to completely span the thickness dimension, which makes the flow pattern almost two-dimensional (2-D) over most of the mold. Only near the nozzle and impingement point is there significant deviation. Down the corner near the impingement point, a weak vortex is formed, as the jet spreads across the narrow face and meets the incoming flow just off the corner along the wide face surface.

B. *Temperature*

The temperature distribution inside the mold is further revealed with longitudinal sections in Figure 4. The isotherms shown in this figure clearly outline the path of the hot steel making up the jet and show how the flow carries heat to the narrow face wall. As the jet moves, it cools and heat diffuses radially away from it due to the strong turbulence. Where the jet impinges the narrow face, it splits to flow both upward and downward. As these flows travel along the mold walls, they continue

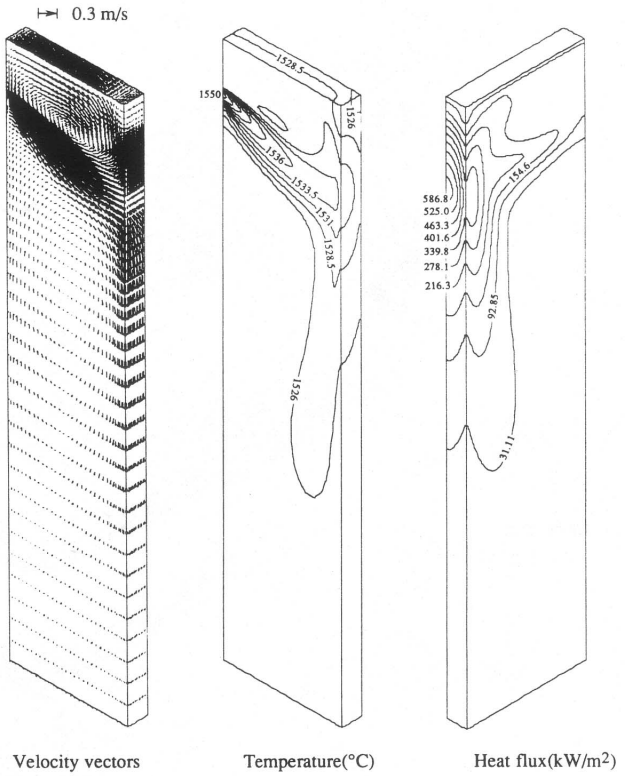

Fig. 2—Fluid flow velocites, temperatures, and heat fluxes predicted by 3-D model (standard conditions, case A in Table I).

to cool against the solidifying steel shell. The steel flowing downward quickly loses its remaining superheat and produces a very cold liquid pool below the jet region. By the time it leaves the computational domain, 3 m below the meniscus, the steel is near the liquidus temperature.

The steel flowing upward also loses most of its superheat by the time it reaches the top surface. The upper recirculation zone delivers the fastest moving, hottest liquid near the center of the molten powder layer (between the nozzle and narrow face). The coldest liquid is found along the narrow face meniscus, particularly near the corner. This is because the liquid in this region has already lost most of its superheat, is traveling very slowly, and is subjected to 3-D cooling through both mold walls and heat loss through the top powder layer.

C. *Heat Flux*

Typical predictions of heat flux leaving the model domain across the liquid/solid shell boundary are presented in Figure 2 as contours over the narrow and wide face surfaces and in Figure 5 as a function of distance down the wall. This heat flux represents the rate of extraction of superheat by the walls and affects growth of the shell, as discussed in Section VIII. These results show that heat flux reaches a maximum at the point where the jet impinges against the walls. This occurs at the center of the narrow face near the bottom of the mold for case A. The maximum reaches 1000 kW/m^2 at about half way down the narrow face for the shallower jet, for the conditions described as case B in Table I.

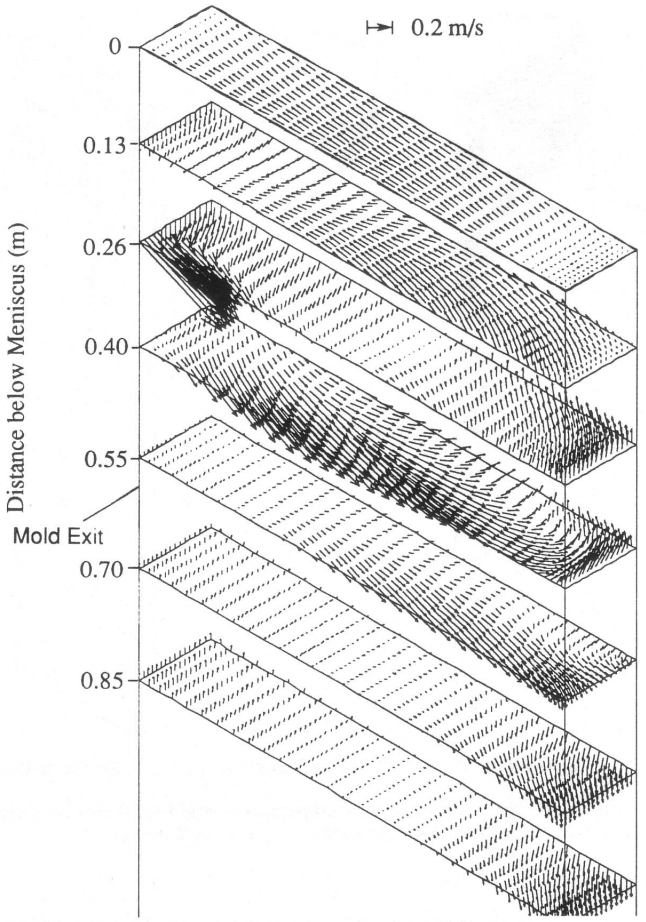

Fig. 3—Predicted velocites in transverse sections down caster.

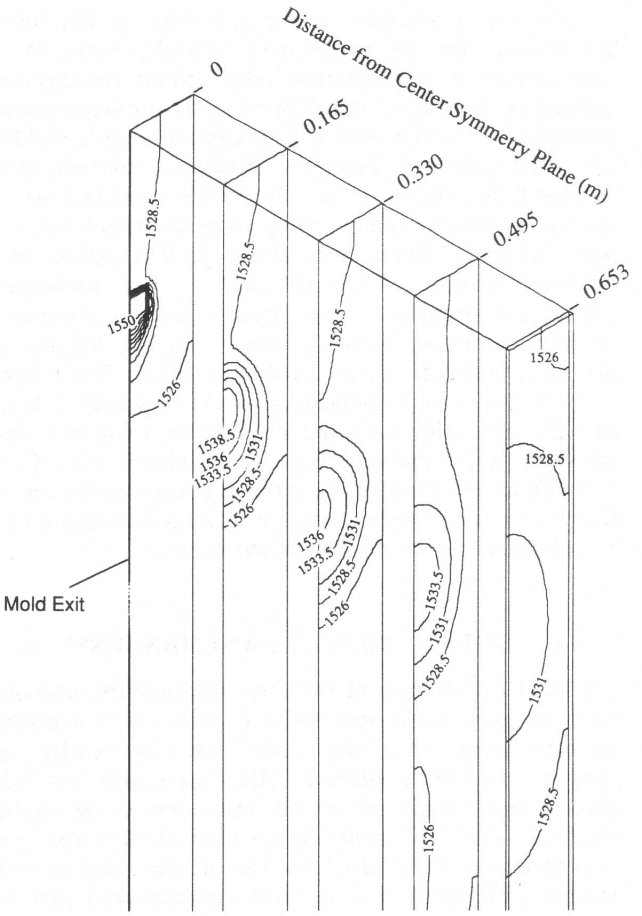

Fig. 4—Predicted temperature contours in vertical sections across caster (°C).

Superheat flux decreases rapidly with distance away from the maximum point in the vicinity of the impingement area. It drops to between 100 and 200 kW/m^2 by the time the liquid reaches the meniscus. The value of this heat flux due to superheat dissipation provides a criterion for the prediction of freezing of the meniscus. When a frozen meniscus is present to generate latent heat, the heat extracted to the mold is larger than the critical value predicted by the model. This is most likely where the superheat flux is small, indicating that very little heat is available to prevent freezing at that location on the meniscus. Alternatively, when the interface temperature is above the liquidus temperature, heat extracted by the mold is smaller. Meniscus freezing is important because it affects depth of oscillation marks, as discussed previously.

Figure 5 shows that the shell moving down the center of the narrow face receives the most superheat, exceeding that of the wide face by several times. The off-corner region of the wide face also experiences a relatively high heat flux, which may contribute to hot-spot formation on the shell surface when this region exits the mold. Heat flux to the corner is somewhat lower for this mold width, but this region is colder due to 2-D heat flow. The center of the wide face receives much less superheat with a greatly different profile. Superheat is extracted by the wide face only near the top of the mold where the shell moves through the upper recirculation zone and past the jet. The peak heat flux is less than one quarter the peak on the narrow face. Below the jet, there is almost no superheat left to extract by the wide face.

Table II presents the distributions of superheat dissipation down the caster, calculated by piecewise integration of the heat flux over each area of the mold surface. This table shows that about 60 pct of the total superheat is dissipated in the mold (narrow and wide faces). This does not include almost 2 pct lost from the top surface through the powder layer. Less than 10 pct of the superheat is convected to deeper than 1.6 m below the meniscus. These results agree with previous estimates that the majority of the superheat is removed in or just below the mold[4] and confirm the importance of superheat indicated by the calculations in Appendix I.

It is interesting to note that more than 30 pct of the superheat is removed in the 1 m directly below the mold. With deeper nozzle submergence or steeper nozzle jet angles, even more of the superheat can be removed in this region and below. This result implies that the efficiency of spray water cooling in the first spray zone segment below the mold is especially critical, because the shell is very thin and hot and a lot of superheat must still be removed. This is particularly important on the narrow face and edges of the wide face, which receive much more than a proportional share of this superheat, as previously discussed. The combination of inadequate or nonuniform sprays at this location where the shell is its

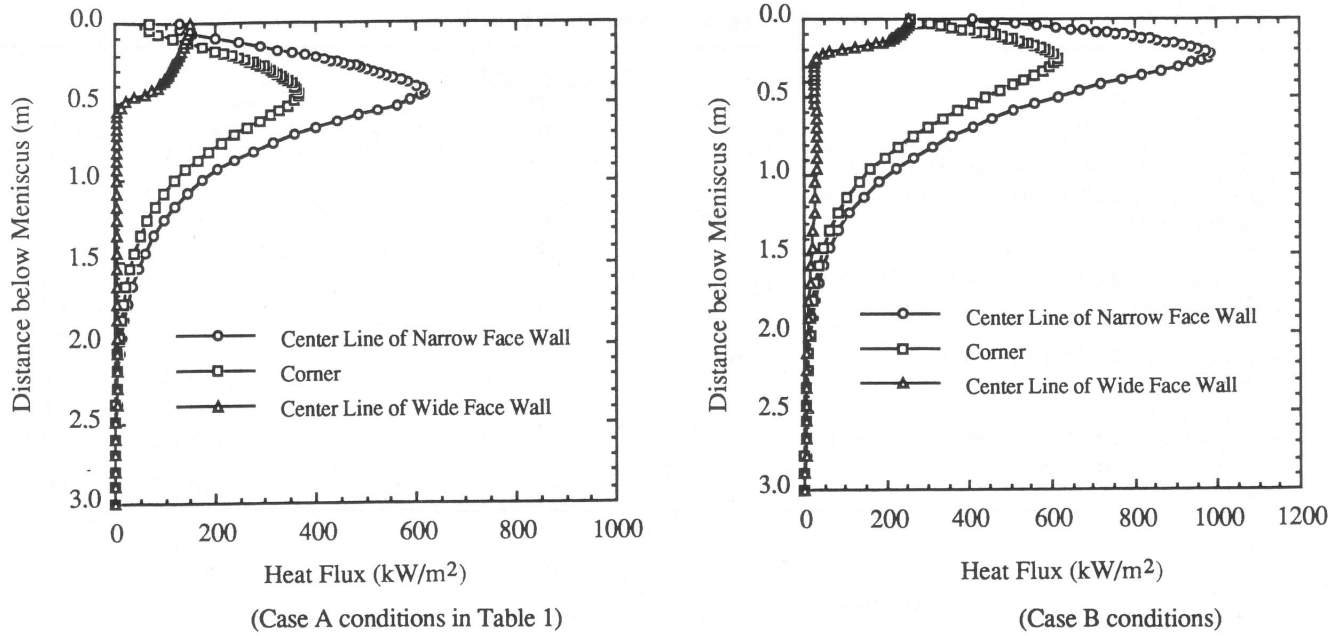

Fig. 5—Heat flux from liquid to solidifying steel shell at various positions.

thinnest, hottest, and weakest would increase the likelihood of breakouts, bulging, and distortion of the unsupported shell just below mold exit.

D. *Effect of Model Dimensions*

Figures 6 and 7 compare the velocity and temperature results calculated by the 3-D model at the centerplane of the mold with results calculated using a 2-D finite element model under the same conditions. The 2-D calculations were performed on a 75 × 40 mesh of 2-D four-node finite elements using the commercial code, FIDAP, as described elsewhere.[14] Because the bifurcated nozzle sends flow into the plane of a relatively thin cavity, the resulting flow pattern is relatively uniform through the thickness of the mold over most of the mold interior, as seen in Figure 3. Thus, the 3-D flow pattern can be reasonably approximated with a 2-D model of a vertical section through the mold parallel to the wide face, as seen in Figure 6. The only major difference between the two flow patterns is the increased upward curvature of the jet in the bulk of the mold in the 3-D results. This produces a slightly higher impingement point on the narrow face wall for the 3-D calculations. The curvature is likely caused by the upward lifting force on the jet resulting from the reduced pressure in the upper recirculation zone. Because the 2-D jet broadens less, it has more momentum to resist this upward bending.

The temperature results are qualitatively similar, but Figure 7 shows that the 2-D temperatures are naturally hotter because heat losses through the wide faces are neglected. Figure 8 compares the 2-D model heat flux predictions with 3-D results down the center of the narrow face. To compensate for neglecting heat loss to the wide face, the 2-D model results were scaled down to 30 pct, the typical fraction of heat actually lost through the narrow face. The 2-D heat flux profile is then similar to the 3-D prediction. In conclusion, the 2-D model appears to be a very reasonable approach to simulating flow in the mold, owing to its greatly reduced computational cost.

E. *Effect of Mesh Refinement*

Initial runs were conducted using a coarser 30 × 24 × 9 mesh. This mesh converged very fast and produced qualitatively similar results to both the present 3-D and 2-D models. However, the lower recirculation zone was very shallow and severely skewed so that its center was much closer to the nozzle (*i.e.*, higher and toward the caster center symmetry plane). The mesh was refined to the present 60 × 34 × 16 grid, which is believed to produce a reasonable, converged solution.

F. *Effect of Wall Roughness*

A wall roughness parameter, E, of 0.8 was calculated based on a maximum average variation of wall surface height of 7.5 mm,[25] which corresponds to the width of the mushy zone. The effect of this roughness parameter on the heat flux profile down the center of the narrow face is shown in Figure 9. This figure shows that increasing the roughness parameter from its nominal value of 0.8 for the rough wall to 8.8 for a smooth wall has only a small effect. Its influence on the flow pattern and temperature distribution is smaller. The deep crevices that comprise the inner surface of the dendrites in the continuous caster promote slightly faster local heat dissipation relative to the flat surface of a smooth wall. This creates a slightly sharper heat flux peak at the impingement point, with less superheat flux left to remove lower down.

G. *Effect of Thermal Buoyancy*

To investigate the importance of the thermal buoyancy forces, a single simulation was performed to solve for

Table II. Predicted Superheat Distribution

Superheat Lost To:	Case A Heat Flow (kW)	Case A Percent	Case B Heat Flow (kW)	Case B Percent
Conduction through top surface flux layer	11	2	9	1
Convection to shell inside mold (0 to 0.6 m)				
Narrow face	97	17	176	21
Wide face	249	43	299	35.5
Convection to shell just below mold (0.6 to 1.6 m)				
Narrow face	66	11	84	10
Wide face	115	20	201	24
Convection to shell farther below mold (1.6 to 3.0 m)				
Narrow face	5	1	8	1
Wide face	36	6	60	7
Dissipation very low in caster (below 3.0 m)	4	1	4	0.5
Numerical convergence errors	− 1	0	− 1	0
Total	582	100	840	100

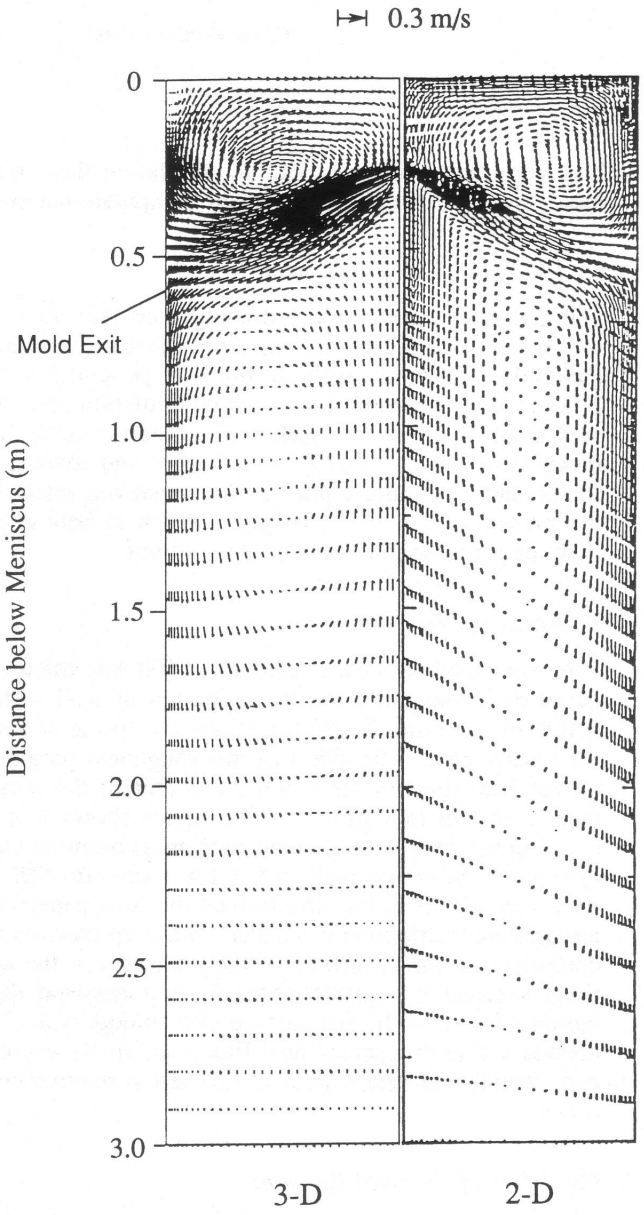

Fig. 6—Comparison of 3-D and 2-D velocity predictions in centerline section through caster.

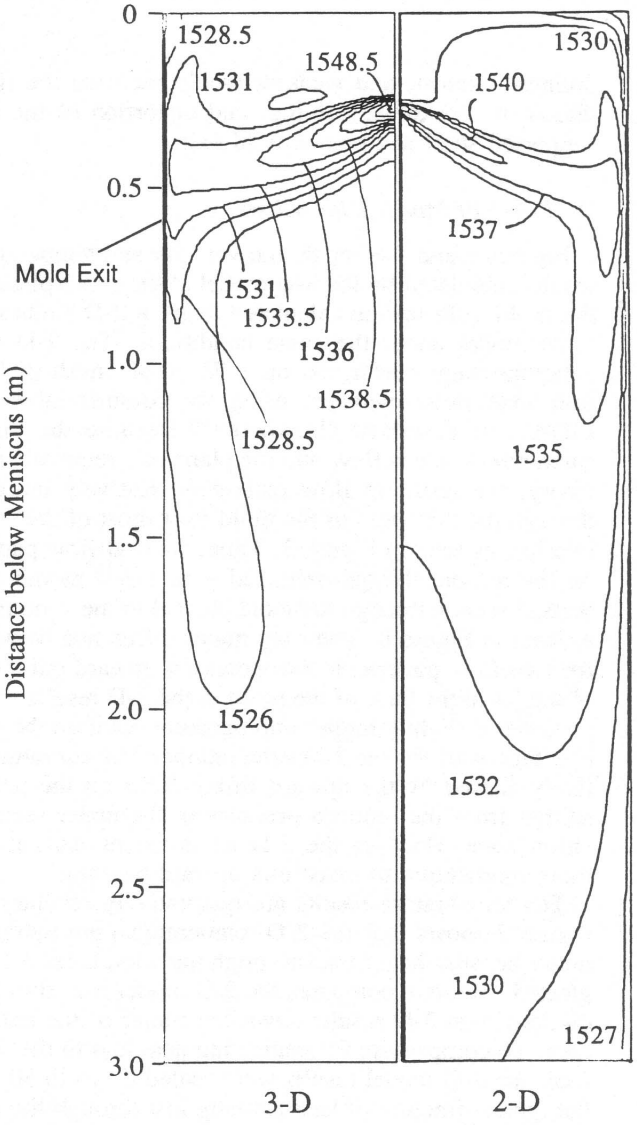

Fig. 7—Comparison of 3-D and 2-D temperature predictions in centerline section through caster (°C).

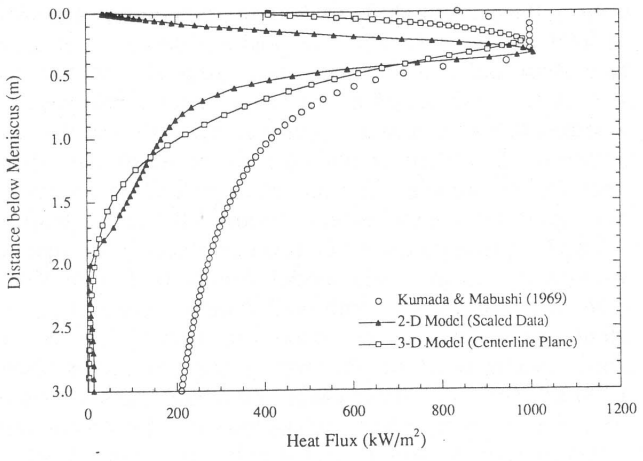

Fig. 8—Comparison among model heat flux predictions and experimental correlations (case B conditions).[1]

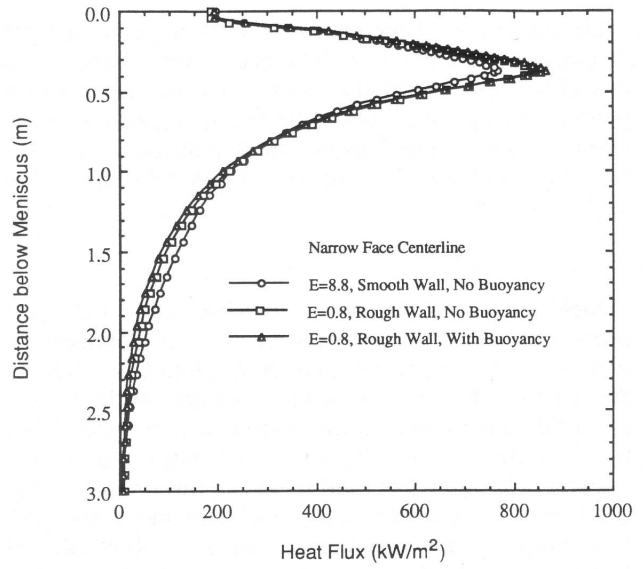

Fig. 9—Effect of thermal buoyancy and wall roughness on superheat dissipation (case A conditions with 1.8 m/min casting speed).

the coupled velocity and temperature fields including this effect. This involved a new force term in the momentum equations, f_z, defined in Appendix II. The heat flux profiles in Figure 9 illustrate the finding that thermal buoyancy forces are not very important in the mold, producing no significant change in either the velocity or temperature fields. This result is expected, because the inertia of the liquid entering rapidly through the nozzle exceeds the thermal buoyancy forces. Later, when the jet has slowed down enough to be affected by secondary forces, its superheat has been dissipated and there is little temperature difference to drive the flow. The dominance of the inertial forces on flow in the upper liquid pool can be seen through evaluation of the modified Froude number, Fr*, (Table I). This dimensionless quantity represents the ratio between inertial and thermal buoyancy forces,

$$\mathrm{Fr}^* = \frac{v^2}{gL\beta\Delta T_s} \qquad [4]$$

Inserting a typical velocity in the upper mold of 0.3 m/s and taking other values, such as mold half width, from Table I, yields Fr* = 5. This suggests that inertial forces are at least five times more important than buoyancy forces in controlling the flow pattern. In addition, turbulent mixing promotes uniform composition, avoiding solute-driven flow. Thus, it appears reasonable that the jet position, which controls the overall flow pattern and accompanying heat transfer in the mold, should not depend much on buoyancy phenomena.

In the stagnant regions both in and below the mold, however, the flow becomes more complicated. Natural convection becomes an important force driving flow down near the walls, where Fr* is small. At the same time, solute rejection by the dendrites lowers the density of the adjacent liquid steel and tends to drive flow upward in the stagnant regions near the solidifying front. Thus, the model must be greatly enhanced before accurate predictions can be made in these regions where forced convection from the inlet jet has vanished, such as the vicinity of the mushy region lower down the strand. For the purposes of this work, which concerns macroscopic heat transfer in the mold, natural convection appears not to be important.

This finding contrasts with flow in the tundish, where thermal buoyancy has been found to be very important, owing to the unforced, slower velocities through a larger vessel with similar temperature differences.[26] We estimate the Fr* in the critical high-velocity regions of the tundish, where buoyancy forces change the flow pattern, to be about 0.4, more than 10 times smaller than corresponding values in the mold.

V. MODEL VERIFICATION

A. *Velocity*

The predicted flow patterns (both 2-D and 3-D) are very similar to flow observed in a physical water model of the mold under the same conditions.[15] Favorable comparisons have also been made with hot-wire anemometer measurements of velocity.[16,17] However, numerical studies indicate that the velocity pattern is the least sensitive variable of concern.[14]

B. *Temperature*

The centerplane temperature predictions of the 3-D model are compared in Figure 10 with thermocouple measurements in the molten steel from Offerman.[21] To achieve the comparison, the standard model conditions were altered to set T_0 = 1540 °C and T_{liq} = 1510 °C. Overall agreement is reasonable, as the same general trends outlined above can be seen in the measurements. The only qualitative difference is a slight drop in liquid temperature measured at the top surface near the nozzle. This might have been missed by the 3-D model predictions due to false numerical diffusion, inherent to finite difference calculations, that would enhance conduction to this area.

Quantitatively, measured temperatures are somewhat colder in the central region of the liquid pool than calculated by the 3-D model. In particular, the measured

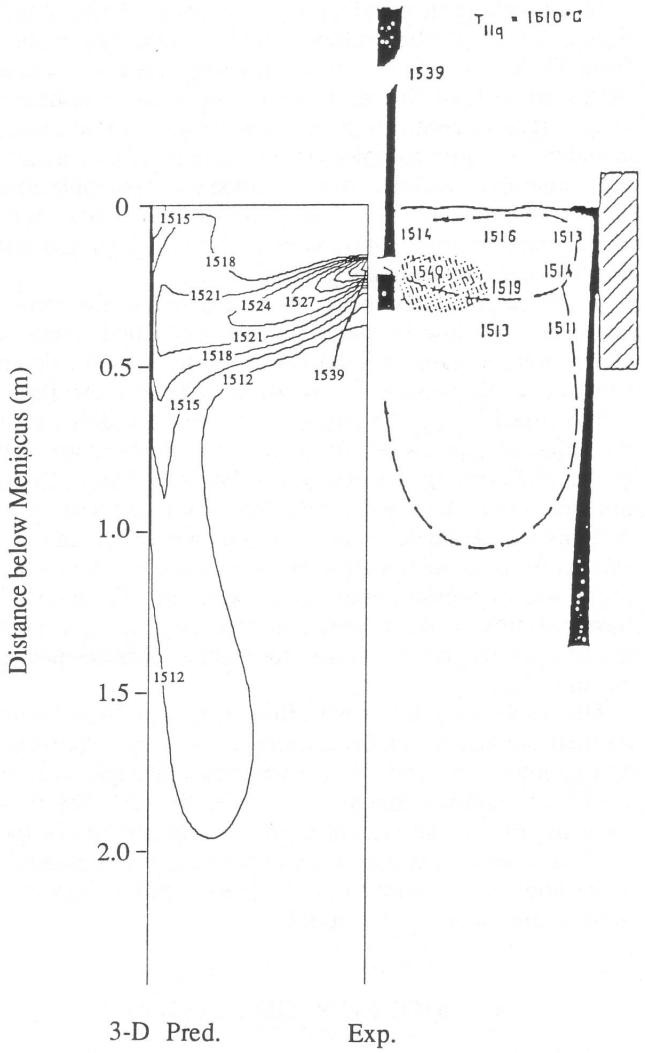

Fig. 10—Comparison of calculated (3-D model) and measured[21] molten steel temperatures (°C).

temperature of the jet drops from 1540 °C to 1519 °C, losing two thirds of its superheat, while traveling only half way across the mold. The model predicts that the jet does not cool this much until very near its impingement point on the narrow face wall. This discrepancy might be caused by the melting of dendrites broken off the inside of the shell.[21,27] Alternatively, there may have been problems locating the hottest part of the jet when making the experimental measurements. Differences in thermocouple location of 50 mm or less would account for the discrepancies. Finally, the assumed Pr_t of 0.9 might be too high. A lower value of Pr_t would enhance turbulent diffusion, thereby lowering temperature everywhere in the mold.

C. *Heat Flux*

Model heat flux predictions have been compared with calculations based on experimental measurements of water jet impingement on a heated flat plate, correlated by Kumada and Mabuchi.[28] These correlations were adapted to predict heat transfer due to steel jet impingement within a continuous casting mold.[1,14] The same method was used in the present study to find an independent estimate of heat flux as a function of position down the narrow face shell wall. In this procedure, heat flux lost to the wall is first calculated at the point of jet impingement, as a function of the total superheat. Heat flux in the two adjacent regions are calculated next, based on the superheat still remaining. This recursive procedure continues both up and down the mold to produce the entire profile.

The heat flux predicted by this correlation is compared with both 2-D and 3-D model results in Figure 8 for case A, assuming a smooth wall. There is general agreement, particularly for the maximum heat flux at the jet impingement point on the narrow face, which is about 1000 kW/m^2 in all three cases. This heat-transfer rate is comparable with rates measured by Sismanis and Argyropoulos for solid steel melting in a stirred liquid steel bath.[29]

VI. EFFECT OF CASTING CONDITIONS

Having explored the characteristics of the model predictions and attempted to demonstrate their validity, the model was next applied to investigate the effect of important casting variables on the rate of superheat extraction and temperature distribution. Conditions were based on case A in Table I using the 3-D model unless otherwise mentioned.

A. *Steel Grade*

Steel grade was assumed to affect only the liquid properties: density, specific heat, thermal conductivity, and viscosity. These variables have almost no effect on the results. This is because only changes in the laminar properties were investigated. Turbulence dominates both the flow (through the turbulent viscosity) and the heat transfer (through the turbulent conductivity). Thus, changes of more than a factor of 4 in the molecular (laminar) viscosity and conductivity have no observable effect on either the flow or heat transfer. Physical models traditionally assume that the turbulent properties increase in direct proportion to the laminar ones, allowing scaling between fluids with known differences in laminar properties. However, further studies into this were not conducted because the turbulent properties of liquid metals are not known well enough to properly modify the parameters in the turbulence equations. It is strongly suspected that the effect of steel grade is always small.

B. *Superheat Temperature*

Superheat temperature, ΔT_s, has the most direct influence on superheat dissipation of all casting variables. Because natural convection in the mold is negligible, superheat temperature does not affect the flow pattern in the mold. Thus, superheat delivered to the shell increases in direct proportion to the difference between the liquidus and pouring temperatures. This trend is illustrated in Figure 11, which shows the expected linear increase in heat flux to the narrow face with increasing ΔT_s, calculated by the model. Because the fraction of heat extracted by the mold is unaffected, higher superheats result in thinner shells leaving the mold. Thus, accommodations should be made when casting with a high

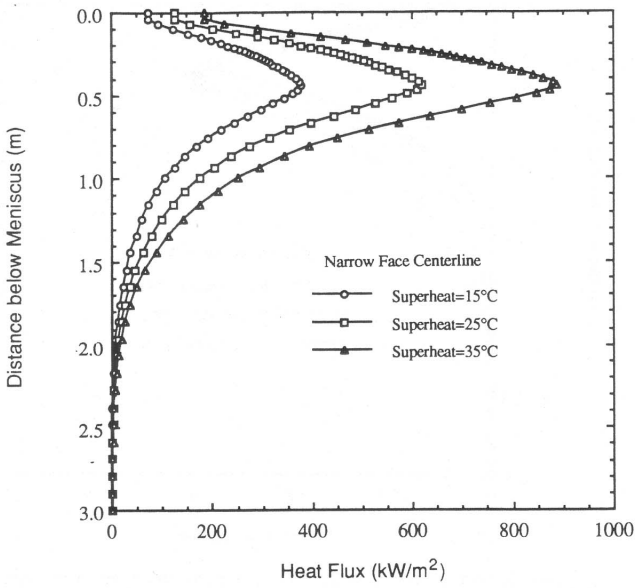

Fig. 11—Effect of superheat temperature difference on superheat dissipation.

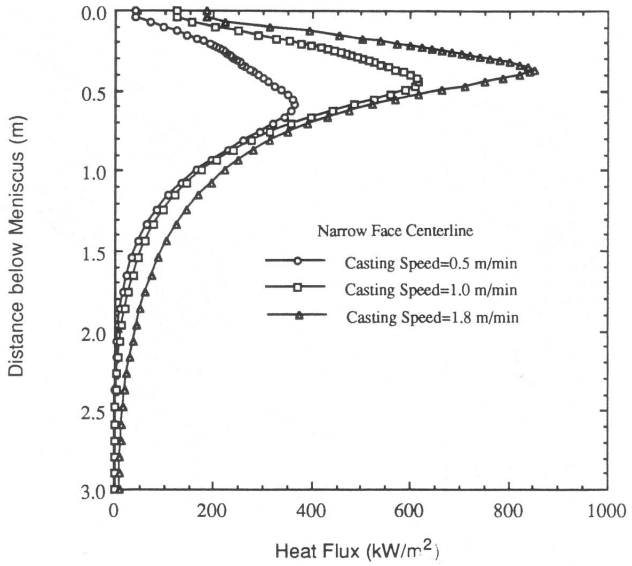

Fig. 12—Effect of casting speed on superheat dissipation.

superheat, to avoid breakouts. Higher superheat also increases the temperature gradient at the solidifying interface, which promotes a columnar grain structure.

C. *Casting Speed*

The importance of casting speed on superheat dissipation can be inferred from its definition in Eq. [1] and Appendix I. This equation shows that the superheat to extract increases in direct proportion with the casting speed. To investigate this important casting variable, the 3-D model was run with three different casting speeds, obtained by increasing the velocity through the same area of inlet port.

In general, casting speed has little qualitative effect on either the velocity or temperature fields. However, the magnitudes of velocity, temperature, and heat flux all increase significantly with speed. The results in Figure 12 confirm that increasing casting speed greatly increases heat flux to the inside of the narrow face. This finding is consistent with the increase in heat-transfer rate encountered when fluid velocity across the solidifying interface is increased that has been observed experimentally in stirring of liquid metal baths.[29]

This figure also shows that the heat flux peak sharpens and a slightly lower fraction of the superheat is removed by the narrow face at higher casting speeds. This is because the higher average velocities cause slightly more of the superheat to be convected to the wide face before the jet reaches the impingement point. This lowers the fraction of superheat removed by the narrow face slightly, from 31 pct at 0.5 m/min to 27 pct at 1.8 m/min. The total fraction of the superheat extracted in the mold remains the same at about 60 pct. Thus, problems related to superheat extraction become an increasing concern at higher casting speeds.

These problems could be a concern even at a moderate casting speed, if a nozzle port becomes severely blocked by alumina buildup, and increases the flow through the other port. This would result in jet impingement on one narrow face equivalent to that experienced at a much higher casting speed.

Casting speed and superheat temperature both increase the heat flux directly, so it appears important to control these two variables together to avoid problems associated with excessive superheat delivery to the narrow face region. Specifically, a reduced casting speed should be used when very high superheats are encountered. A maximum safe casting speed likely exists for each superheat. The exact relationship should depend on the other casting variables, including nozzle angle and submergence depth.

D. *Mold Width*

The model was next run to investigate the effect of mold width on superheat extraction rate, assuming a constant casting speed. In order to keep the casting speed constant, a higher flow rate is required through the nozzle for wider slabs. The resulting higher velocities tend to increase the heat flux, as discussed in Section C. Figure 13 presents contours of surface heat flux for two different mold widths, and Figure 14 compares the heat flux profiles to the narrow face centerline. The magnitude and location of the heat flux peak on the narrow face are similar (within 10 pct) for all widths. More heat is extracted from the narrow face and off-corner regions of wider molds, however, as the greater heat flux contours in Figure 13 spread over a larger region of the wider mold. In addition, more of this heat is extracted below mold exit, so there is a greater danger of shell thinning in the first spray zone for wider slabs. These findings are expected, because the jet must carry more heat through a wider mold, as seen in Eq. [1].

The dangers of high superheat extraction to the shell do not increase in direct proportion to mold width, because the wide face surface area increases and the jet must travel further through a wider mold. The fraction of the superheat leaving the narrow face decreases from

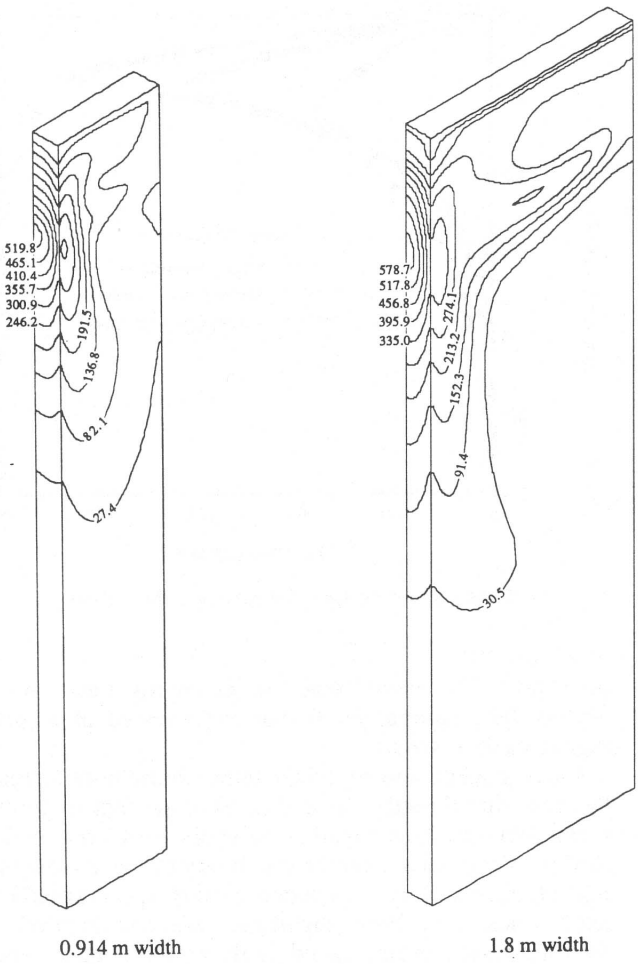

Fig. 13—Effect of mold width on superheat dissipation (kW m^{-2}).

32 to 23 pct as width increases from 0.914 to 1.83 m. At the same time, the fraction of heat extracted below the mold decreases from 46 to 38 pct.

Figure 13 shows that the distribution of superheat to the wide face also changes. In narrow molds, heat extraction to the wide face is highest very near the narrow face. In wide molds, however, the jet, which is spread completely across the mold thickness, directly contacts the wide face for a longer distance, cooling the jet significantly. Heat losses to the wide face thus reach their peak before the jet gets to the narrow face.

E. *Jet Angle*

The angle of the steel jet is controlled by the nominal angle, size, and thickness of the nozzle outlet ports.[15,20,25] When oversized, thin-walled, downward ports are used, the impingement point on the narrow face is usually just above mold exit. Altering the nozzle geometry to produce a shallower or upward flowing jet moves the impingement point slightly higher up the narrow face wall. Figure 15 shows how the temperature distribution through the centerplane changes with jet angle. The peak heat flux moves higher up the narrow face centerline in a corresponding manner, as shown in Figure 16. At the same time, a smaller fraction of the superheat is removed below the mold. Thus, heat extraction in the first spray zone is somewhat less of a concern for shallow nozzles.

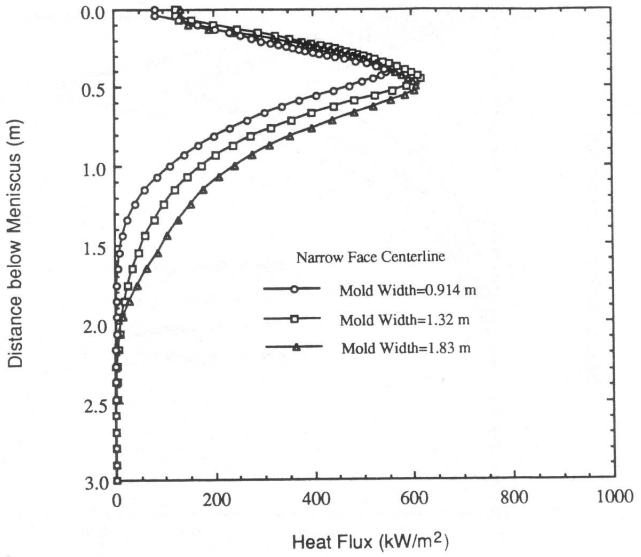

Fig. 14—Effect of mold width on superheat dissipation to narrow face centerline.

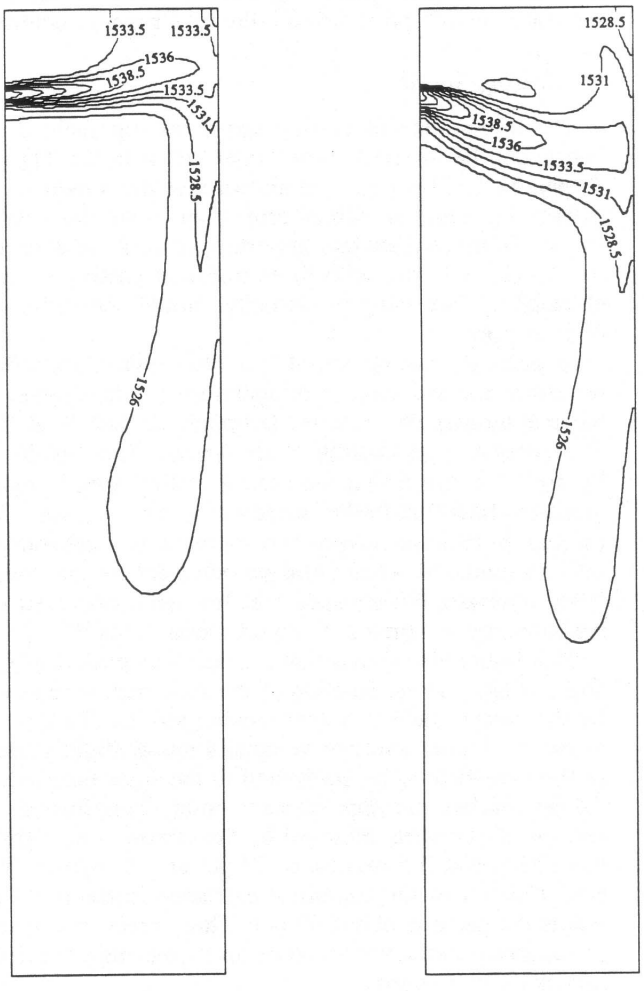

Fig. 15—Effect of jet angle on centerplane temperature distribution (°C).

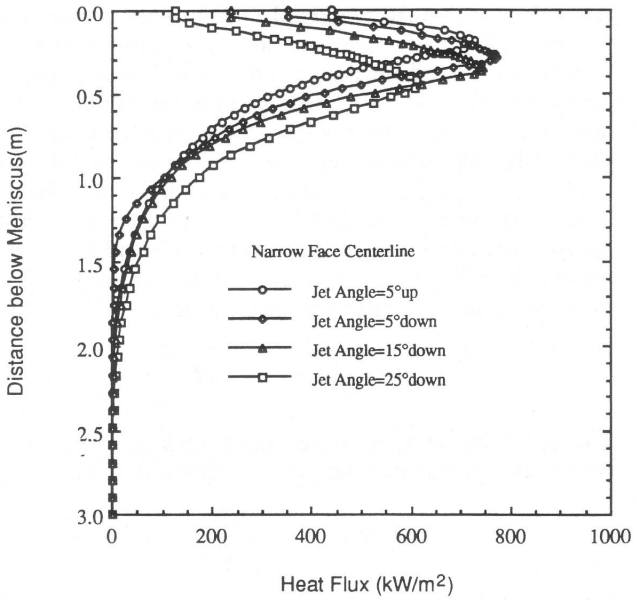

Fig. 16—Effect of jet angle on superheat dissipation.

Even more important than the location of the maximum heat flux is the rate of heat extraction at the meniscus, which controls meniscus freezing. Shallow or upward nozzles send hotter liquid to the meniscus, as shown in Figure 15. Figure 16 shows that the critical meniscus heat flux rises from 150 to 400 kW/m^2 as nozzle angle changes from 25 deg down to 5 deg up. The problems of meniscus freezing and accompanying deep oscillation marks therefore decrease with shallower nozzle jets, because heat extraction from the steel to the mold is less likely to exceed this critical value. Meniscus freezing problems are also predicted to be less for higher superheat temperatures and casting speeds, as indicated in Figures 11 and 12 by the higher meniscus heat fluxes under these conditions.

Too great an upward-pointing jet angle can produce a radical change in flow pattern, when a shallow submergence depth is used in a wide mold.[30] Under these detrimental conditions, the flow impinges first upon the top surface of the liquid. This produces excessive surface turbulence, a smaller upper recirculation zone, and very different temperature and heat flux profiles. The present simulations represent typical operating conditions with relatively deep submergence, where this does not occur.

F. *Submergence Depth*

When the liquid jet leaving the nozzle points downward, then changing the nozzle submergence depth changes the point of impingement on the narrow face wall in direct proportion. Figure 17 shows the expected trend that the heat flux profile shifts downward by about the same distance (0.2 m) that the nozzle submergence was lowered from 0.15 to 0.365 m. This figure was produced with the 2-D model for case B conditions, with the results scaled down to 32 pct to account for heat leaving the wide face according to Table II. Note that the predicted narrow face heat flux is greater for the conditions of case B, relative to A, owing to the higher casting speed and wider mold.

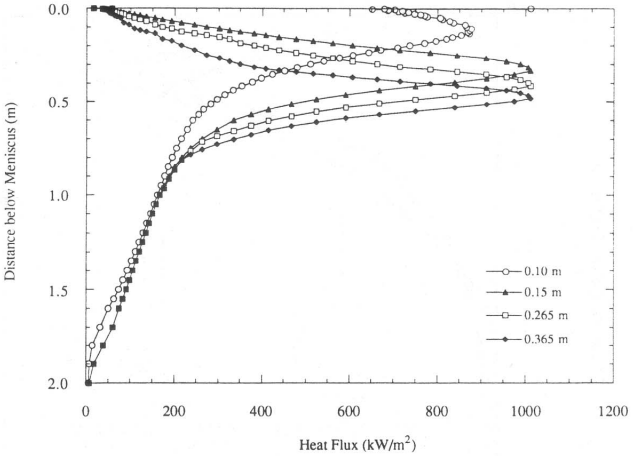

Fig. 17—Effect of nozzle submergence depth on superheat dissipation from scaled 2-D calculations (case B conditions).

Deeper submergence was found to deliver colder fluid to the top surface of the liquid pool, producing the same problems found with steep downward nozzle angles. Shallower submergence shifts the heat flux profile up the wall. Eventually, too shallow a submergence makes the jet first impinge on the top surface at a combination of critical submergence depth and nozzle angle. This produces heat input to the meniscus in excess of 600 kW/m^2, close to the peak narrow face value, as seen in Figure 17 for 0.10-m submergence depth. The effect is very similar to that obtained when the jet angle from an upward nozzle is too high. Although the high rate of meniscus heat transfer should decrease problems associated with meniscus freezing, the problems generated by the surface turbulence are more damaging. Thus, more quality problems, such as longitudinal cracks, are observed at shallow submergence depths.[31]

G. *Jet Inlet Profile*

Figure 18 shows the effect of jet inlet profile on the heat flux profile down the narrow face centerline. The true inlet profile entering the mold is close to a semiparabola entering through only the bottom half of the port height.[15] The profile can be simplified to a constant velocity through a taller inlet port, while maintaining the same mass flow and casting speed. In this case, however, the average inlet velocity is lower, so less turbulence is generated. This results in less turbulent transport, less diffusion, and less loss of the heat carried by the jet between the mold wide faces. This produces a higher, sharper peak heat flux at the impingement point on the narrow face. The fraction of superheat removed by the narrow face remains about the same, however.

VII. SOLIDIFICATION MODEL

The relationship between the heat flux calculated from superheat dissipation and the heat extracted to the mold wall is illustrated schematically in Figure 19 for the narrow face. Growth of the shell naturally depends upon the combination of these two boundary conditions. The superheat distribution is important, as this figure shows

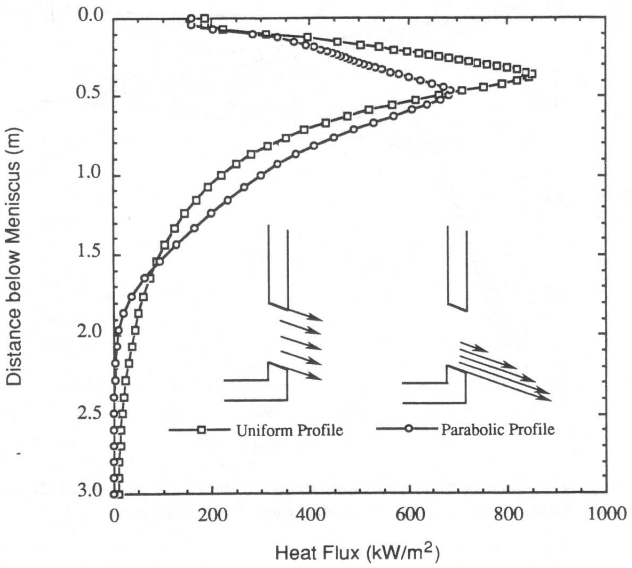

Fig. 18—Effect of inlet velocity profile on superheat dissipation (narrow face centerline).

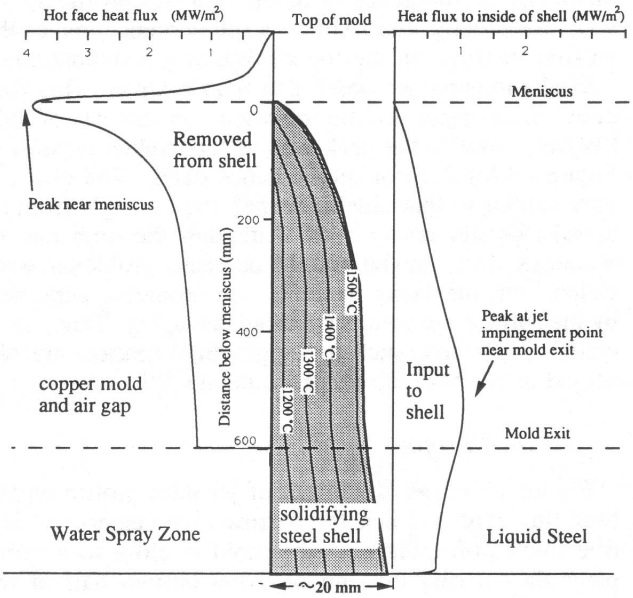

Fig. 19—Schematic of heat transfer through solidifying steel shell (narrow face).

that the two curves are of the same magnitude. To determine the importance of the variation in superheat delivered to the narrow and wide faces on temperature development and growth of the solidifying steel shell, a simple solidification model was developed.

The general partial differential equation governing heat conduction in the continuously cast strand is

$$\rho_s\left(\frac{\partial H}{\partial t} + V_z\frac{\partial H}{\partial z}\right) = \frac{\partial}{\partial x}\left(k_s\frac{\partial T}{\partial x}\right) + \frac{\partial}{\partial y}\left(k_s\frac{\partial T}{\partial y}\right) + \frac{\partial}{\partial z}\left(k_s\frac{\partial T}{\partial z}\right) \quad [5]$$

Velocity in the x and y directions in the solid shell is zero. As commonly practiced,[8] this work assumes the process is at steady state and adopts a Lagrangian frame of reference fixed on the strand moving at constant velocity (so $V_z = \partial z/\partial t$). Heat conduction in the casting direction (z dimension) is negligible relative to the heat carried by the strand movement, because the relevant ratio, $k_s/(\rho_s C_{ps} V_z L_m)$, is only about 0.0003. In addition, conduction across the mold (y direction) is negligible, because the shell is so thin relative to its width. Finally, the latent heat of fusion, ΔH_L, in the enthalpy, H, is modeled using an effective specific heat, defined as

$$C_{ps}^* = \frac{dH}{dT} = C_{ps} - \Delta H_L\frac{df_s}{dT} \quad [6]$$

The solid fraction, f_s, is assumed to vary linearly between the solidus and liquidus temperatures, so

$$C_{ps}^* = C_{ps} + \frac{\Delta H_L}{T_{liq} - T_{sol}} \quad [7]$$

Equation [5] then simplifies to the one-dimensional (1-D) transient heat-conduction equation,

$$\rho_s C_{ps}^*\frac{\partial T}{\partial t} = \frac{\partial}{\partial x}\left(k_s\frac{\partial T}{\partial x}\right) \quad [8]$$

Temperature dependency of the steel properties, k_s, ρ_s, and C_{ps}, was included but found to have a small effect. Equation [8] is solved at each time step using a finite difference discretization:

$$\text{Interior node: } T_i^{new} = T_i^{old} + \frac{\Delta t\, k_s}{\Delta x^2\, \rho_s\, C_{ps}^*}\cdot(T_{i-1} - 2T_i + T_{i+1}) + q_p\frac{\Delta t}{\Delta x \rho_s C_{ps}^*} \quad [9]$$

$$\text{Surface node: } T_1^{new} = T_1^{old} + \frac{\Delta t\, k_s}{\Delta x^2\, \rho_s\, C_{ps}^*}\cdot(2T_2 - 2T_1) - 2q\frac{\Delta t}{\Delta x \rho_s C_{ps}^*} \quad [10]$$

Subscripts on temperature refer to the node number starting from 1 at the solid surface of the shell, and symbols are defined in Table I. Temperatures at the new time, T^{new}, are solved explicitly from the old temperatures by evaluating all terms in these nodal equations at the old time level. To ensure latent heat is not missed, a post-iterative correction is performed after each time step. Whenever a solidifying node cools below the solidus or a liquid node cools below the liquidus, its temperature is adjusted to account for any incorrect change in enthalpy that occurred during that time step.

Boundary conditions for the model are illustrated schematically in Figure 19. They can be adjusted to simulate lateral positions on either the wide or narrow faces. Heat flux q is extracted from the surface node according to a prescribed function of time or distance down the mold. Below the mold, heat flux is applied as a function

of spray cooling practice (based on water flux) and natural convection (based on a heat-transfer coefficient of 10 W/m^2K).

To describe mathematically how superheat is delivered to the inside of the shell, the initial temperature of every node is set to the liquidus temperature. A function defining heat flux down the mold at the desired position on the mold perimeter, q_p, is taken from the heat flux curves calculated in Section IV, q_{sh}. This q_p function is applied at each time step to the location corresponding to the inside of the shell. This location is presently taken to be the hottest node in the mushy zone (below T_{liq}). At all other nodes, q_p in Eq. [9] is set to zero. A similar method to incorporate superheat is being implemented into a transient thermal-stress model to enable a complete analysis of shell behavior in three dimensions.[22]

VIII. EFFECT OF SUPERHEAT ON SHELL GROWTH

To demonstrate the ability of the solidification model to predict the effect of superheat on shell growth, simulations were conducted for the typical slab casting conditions (case B in Table I), where measurements had also been made.[1] Other values used in the solidification model are given in Table I.

Boundary conditions for heat extraction by the mold, q, were taken from Nakato *et al.*[1] The heat flux for superheat dissipation, q_p, was taken from the fluid flow model results for these conditions, q_{sh}, given in Figure 5 (case B). Shell thickness is defined by linearly interpolating the position between the liquidus and solidus isotherms corresponding to 70 pct solid. Figure 20 compares the solidification model predictions of shell thickness with measurements.[1] The latter were obtained by injecting FeS tracer into the jet stream and taking sulfur prints.

The model results in Figure 20 agree approximately with the measured shell thickness profile down the narrow face. However, the predicted shell growth is smoother, overpredicting shell thickness in the impingement region and under-predicting it lower in the mold. The differences could arise from several sources. First, the thermal properties assumed in the solidification model are important, particularly conductivity in the mushy zone and the solid fraction defining the shell. Some uncertainty exists in the fluid flow computations regarding the possible effect of breaking off dendrite tips, the assumed surface roughness parameter, and other aspects of the wall laws. Alternatively, any variation in the reported hot face boundary conditions, solid diffusion of the FeS tracer, or random fluctuations in shell growth may have produced a particular shell thickness profile that was not exactly representative of the time-averaged profile being calculated.

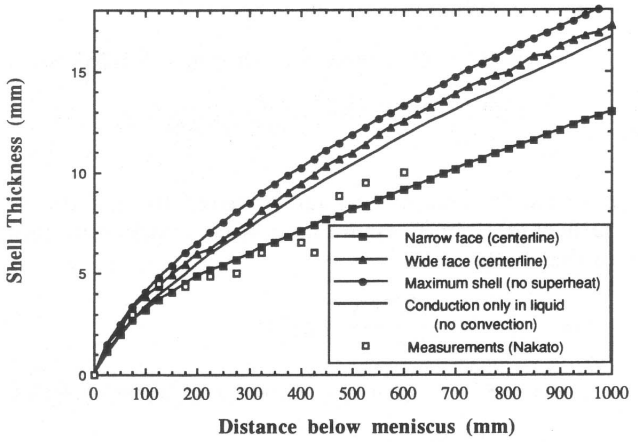

Fig. 20—Calculated shell thickness profiles for wide and narrow faces compared with measurements[1] (case B conditions).

Figure 20 shows that the thick, regular growth of the shell down the wide face is predicted to follow the classical parabolic relationship with time. This curve is similar in shape and close in magnitude to the curve for the maximum shell thickness possible, attained by casting without superheat. This arises from the previous result that relatively little superheat is removed through the wide face.

In contrast, growth of the narrow face shell is significantly slower than the wide face, which agrees qualitatively with the findings of Flint.[3] In addition, its growth is nonuniform, with a sharp reduction in growth rate between about 150 and 450 mm below the meniscus. This coincides with the vicinity of the impingement point of the jet on the shell. Remelting of the shell was not measured or predicted for these conditions. However, a higher casting speed or superheat could produce remelting. This would increase the danger of a breakout, particularly if the shell had an irregular growth pattern with local thin spots, such as due to casting a medium carbon (0.1 pct C) steel grade or deep oscillation marks.

Slight misalignment of the nozzle tube would direct the jet away from the narrow face centers toward the slab corners. This would enhance superheat extraction at the off-corner regions of the wide faces, particularly for narrow slabs. These critical locations would then experience the thinning calculated in Figure 20. Defects found near opposite corners of the slab could be indicators of this potential effect.

The shell growth predicted down the center of the wide face using q_{sh} compares closely with that from a conventional model that assumes only simple heat conduction in the superheated liquid. The best agreement in the mold down the wideface centerline is found with no artificial enhancement of the thermal conductivity in the liquid. Enhancing the conductivity would allow the simple conduction model to approximate other positions down the wide face. This agreement is consistent with the experiences of several previous researchers, who found that this crude approximation is quite successful in predicting average growth of the shell.[8,10]

There is a significant difference in shell thickness down the narrow face, however, between the predictions of the simple conduction model and both the measurements and calculations obtained using q_{sh}, which delivers superheat to the impingement point lower in the mold. The simple conduction model always produces continual removal of superheat down the caster. The result is a slight underprediction of solidification at the meniscus, where the start of solidification is often delayed unnaturally. More significant is a subsequent overprediction of shell growth

near the mold exit on the narrow face and at the adjacent off-corner regions of the wide face. These areas actually remain thinner until considerably below the mold. The discrepancy persists until deep in the caster when all the superheat has been extracted.

The errors in predicting shell thickness could be important, because simple heat conduction models are commonly used to predict the initiation point of defects in the cast slab. For example, an overprediction of shell thickness near the mold exit could imply the cause of a defect was inside the mold, when it actually occurred just below the mold exit. The worst predictions are likely to be found at or near the narrow face, where many defects occur. The differences are also important for understanding subsequent bulging and thermal stress problems.

IX. CONCLUSIONS

A mathematical model has been developed to calculate how superheat is dissipated from the liquid in the continuous slab casting process, based on turbulent 3-D fluid flow and heat transfer. Calculations using a 2-D model are able to approximate many of the 3-D results. The results are input into a solidification model to calculate temperature and growth of the shell. All of the model calculations show at least qualitative agreement with available experimental measurements. The following conclusions are based on these calculations.

More than half of the superheat is removed in the mold. About one third is removed in the first meter of spray zones just below the mold. The narrow face receives much more than a proportional share of the superheat (about one third of the total), while the centerline of the wide face extracts almost none. The maximum heat flux from superheat dissipation is always centered about the point where the jet impinges upon the inside of the steel shell solidifying against the narrow face. This heat flux is almost as great as the heat extracted from the cold side of the shell by the mold. Consequently, growth of the shell down the narrow face and off-corner regions of the wide face is retarded.

Casting speed and superheat temperature both directly increase the superheat extraction rate at the narrow face and off-corner region of the wide face. To avoid problems associated with a thin shell in this vicinity, slower casting speeds should be used when the superheat temperature is very high. Careful attention should be paid to spray water cooling in the first spray zone, particularly at the vulnerable thin-shell regions. Submergence depth, nozzle geometry, and mold width have an important secondary influence. These casting variables should be carefully designed and controlled to produce a flow pattern that delivers steel to the meniscus that is not too cold while avoiding surface turbulence.

Simple solidification models, assuming only heat conduction in the liquid, are able to predict shell growth down the wide face but are less accurate for the narrow face. The differences may be significant in some situations.

The models described in this article are part of a larger system of models being developed to simulate the behavior of the solidifying steel, including the effects of fluid flow, heat transfer, solidification, shrinkage generation, mold distortion, and crack formation are being applied to predict and understand the effects of such diverse variables as nozzle design, mold distortion, and taper on the generation of defects in the solidifying shell. Together, these models should provide a comprehensive analysis tool for the continuous casting process. The goal is to provide insights that will increase understanding of quality problems, such as breakouts, depressions, inclusions, and cracks, and aid in optimizing nozzle and taper design and caster operation.

APPENDIX I

Simple heat balance on typical slab casting mold

For typical casting conditions B (Table I) (0.0267 m/s in a 1.05 × 0.22 × 0.6 m mold):

Rate of heat extracted by mold. Time-average (total) mold heat flux (based on Savage and Pritchard[32]):

$$q_t \approx 2680 - 222\sqrt{\frac{L_m\,(\text{m})}{V_z\,(\text{m/s})}} = 1628\ \text{kW/m}^2 \quad [A1.1]$$

Total heat extracted:

$$Q_{\text{total}} \approx q_t L_m (2W + 2N) = \underline{2481\ \text{kW}} \quad [A1.2]$$

This power comes from the following sources:

Superheat dissipation rate (60 pct of the 27 °C superheat temperature):

$$\begin{aligned} q_{sh} &\approx \Delta T_s \rho C_p V_z \\ &= (27\ ^\circ\text{C})\ (6968\ \text{kg/m}^3)\ (720\ \text{J/kgK})\ (0.0267\ \text{m/s}) \\ &= 3617\ \text{kW/m}^2 \end{aligned} \quad [A1.3]$$

Total superheat: $Q_{sh} = q_{sh} WN = 835$ kW

60 pct of total superheat: $0.6\, Q_{sh} = 501$ kW [A1.4]

Latent heat extraction rate (per unit width and thickness of shell):

$$\begin{aligned} q_{\Delta H_L} &\approx \Delta H_L \rho V_z \\ &= (272{,}000\ \text{J/kg})\ (8000\ \text{kg/m}^3)\ (0.0267\ \text{m/s}) \\ &= 58{,}100\ \text{kW/m}^2 \end{aligned} \quad [A1.5]$$

Sensible heat extraction rate (needed to cool the shell surface to 1250 °C assuming a linear temperature profile in the shell):

$$\begin{aligned} q_c &\approx \left(\frac{T_{\text{liq}} - 1250\ ^\circ\text{C}}{2}\right) \rho C_p V_z \\ &= (1531 - 1250)/2\ (8000\ \text{kg/m}^3)\ (690\ \text{J/kgK}) \\ &\quad \cdot (0.0267\ \text{m/s}) \\ &= 20{,}710\ \text{kW/m}^2 \end{aligned} \quad [A1.6]$$

The rate of heat extraction required to solidify a uniform shell of $X = 10$ mm thick around the entire mold is

$$Q_{\text{wide faces}} \approx (q_{\Delta H_L} + q_c)\,(2W)X = 1655 \text{ kW} \quad [A1.7]$$

$$Q_{\text{narrow faces}} \approx (q_{\Delta H_L} + q_c)\,(2N)X = 347 \text{ kW} \quad [A1.8]$$

$$\text{Total } (Q_{\text{wide faces}} + Q_{\text{narrow faces}} + Q_{sh}) = \underline{2503 \text{ kW}} \quad [A1.9]$$

APPENDIX II

Governing equations for fluid flow

Volume Conservation Equation:

$$\frac{\partial v_x}{\partial x} + \frac{\partial v_y}{\partial y} + \frac{\partial v_y}{\partial z} = 0 \quad [A2.1]$$

Momentum Conservation Equations:

$$\rho\left(v_x\frac{\partial v_x}{\partial x} + v_y\frac{\partial v_x}{\partial y} + v_z\frac{\partial v_x}{\partial z}\right) = -\frac{\partial p}{\partial x} + \frac{\partial}{\partial x}\left(2\mu_{\text{eff}}\frac{\partial v_x}{\partial x}\right) + \frac{\partial}{\partial y}\left(\mu_{\text{eff}}\left[\frac{\partial v_x}{\partial y} + \frac{\partial v_y}{\partial x}\right]\right) + \frac{\partial}{\partial z}\left(\mu_{\text{eff}}\left[\frac{\partial v_x}{\partial z} + \frac{\partial v_z}{\partial x}\right]\right) \quad [A2.2]$$

$$\rho\left(v_x\frac{\partial v_y}{\partial x} + v_y\frac{\partial v_y}{\partial y} + v_z\frac{\partial v_y}{\partial z}\right) = -\frac{\partial p}{\partial y} + \frac{\partial}{\partial x}\left(\mu_{\text{eff}}\left[\frac{\partial v_y}{\partial x} + \frac{\partial v_x}{\partial y}\right]\right) + \frac{\partial}{\partial y}\left(2\mu_{\text{eff}}\frac{\partial v_y}{\partial y}\right) + \frac{\partial}{\partial z}\left(\mu_{\text{eff}}\left[\frac{\partial v_y}{\partial z} + \frac{\partial v_z}{\partial y}\right]\right) \quad [A2.3]$$

$$\rho\left(v_x\frac{\partial v_z}{\partial x} + v_y\frac{\partial v_z}{\partial y} + v_z\frac{\partial v_z}{\partial z}\right) = -\frac{\partial p}{\partial z} + \frac{\partial}{\partial x}\left(\mu_{\text{eff}}\left[\frac{\partial v_z}{\partial x} + \frac{\partial v_x}{\partial z}\right]\right) + \frac{\partial}{\partial y}\left(\mu_{\text{eff}}\left[\frac{\partial v_z}{\partial y} + \frac{\partial v_y}{\partial z}\right]\right) + \frac{\partial}{\partial z}\left(2\mu_{\text{eff}}\frac{\partial v_z}{\partial z}\right) + \rho f_z \quad [A2.4]$$

Turbulence Equations:

$$\rho\left(v_x\frac{\partial K}{\partial x} + v_y\frac{\partial K}{\partial y} + v_z\frac{\partial K}{\partial z}\right) = \frac{\partial}{\partial x}\left(\frac{\mu_{\text{eff}}}{\sigma_k}\frac{\partial K}{\partial x}\right) + \frac{\partial}{\partial y}\left(\frac{\mu_{\text{eff}}}{\sigma_k}\frac{\partial K}{\partial y}\right) + \frac{\partial}{\partial z}\left(\frac{\mu_{\text{eff}}}{\sigma_k}\frac{\partial K}{\partial z}\right) + \rho G_K - \rho\varepsilon \quad [A2.5]$$

$$\rho\left(v_x\frac{\partial \varepsilon}{\partial x} + v_y\frac{\partial \varepsilon}{\partial y} + v_z\frac{\partial \varepsilon}{\partial z}\right) = \frac{\partial}{\partial x}\left(\frac{\mu_{\text{eff}}}{\sigma_\varepsilon}\frac{\partial \varepsilon}{\partial x}\right) + \frac{\partial}{\partial y}\left(\frac{\mu_{\text{eff}}}{\sigma_\varepsilon}\frac{\partial \varepsilon}{\partial y}\right) + \frac{\partial}{\partial z}\left(\frac{\mu_{\text{eff}}}{\sigma_\varepsilon}\frac{\partial \varepsilon}{\partial z}\right) + c_1\frac{\varepsilon}{K}\rho G_K - c_2\frac{\varepsilon}{K}\rho\varepsilon \quad [A2.6]$$

where $\mu_{\text{eff}} = \mu_0 + \mu_t$ = effective viscosity (kg m^{-1} s^{-1});

$\mu_t = c_\mu\rho\dfrac{K^2}{\varepsilon}$ = turbulent viscosity (kg m^{-1} s^{-1});

$$G_K = \frac{\mu_t}{\rho}\left[2\left(\frac{\partial v_x}{\partial x}\right)^2 + 2\left(\frac{\partial v_y}{\partial y}\right)^2 + 2\left(\frac{\partial v_z}{\partial z}\right)^2 + \left(\frac{\partial v_x}{\partial y} + \frac{\partial v_y}{\partial x}\right)^2 + \left(\frac{\partial v_x}{\partial z} + \frac{\partial v_z}{\partial x}\right)^2 + \left(\frac{\partial v_z}{\partial y} + \frac{\partial v_y}{\partial z}\right)^2\right]$$

= turbulence generation rate (m^2 s^{-3})

$c_1 = 1.44$, $c_2 = 1.92$, $c_\mu = 0.09$, $\sigma_K = 1.0$, $\sigma_\varepsilon = 1.3$;

p = static pressure (Pa);

v_i = liquid velocity component in i direction ($i = x$, y, or z) (m s^{-1})

z = distance below meniscus (top surface) (m); and

f_z = gravitational acceleration = $g = 9.81$ (m s^{-2})
= $g + \beta(T_0 - T)g$ when thermal buoyancy is considered.

APPENDIX III

Wall law boundary conditions

The following set of well-known wall function approximations are imposed on the near-wall grid nodes to account for the steep velocity gradients near a wall.[19]

for $y_+ > 11.5$

$$\tau_w = v_t\left(\rho K^{1/2} c_\mu \kappa \frac{1}{\ln (Ey_+)}\right) \quad [A3.1]$$

$$K = (c_\mu)^{-1/2}\frac{\kappa^2 v_t^2}{\ln (Ey_+)} \quad [A3.2]$$

$$\varepsilon = (c_\mu)^{3/4} K^{3/2}\frac{\ln (Ey_+)}{\kappa y_n} \quad [A3.3]$$

for $y_+ \le 11.5$

$$\tau_w = (c_\mu)^{1/2}\rho K \quad [A3.4]$$

$$K = (c_\mu)^{-1/2}\left(\frac{v_t^2}{y_+^2}\right) \quad [A3.5]$$

$$\varepsilon = (c_\mu)^{1/2} K\frac{v_t}{y_n} \quad [A3.6]$$

where $y_+ = (c_\mu)^{1/4} \frac{\rho y_n}{\mu_0} K^{1/2}$;

v_t = liquid velocity component tangential to the wall (m s^{-1});

τ_w = shear stress at the wall = $\mu_{\text{eff}} \frac{\partial v_t}{\partial n}$ (Pa); and

n = direction perpendicular to wall.

Heat flux through the vertical edges of the computational domain near the narrow and wide faces is calculated from the temperature solution *via*

$$q_{sh} = \frac{\rho C_p (T - T_{\text{liq}}) (c_\mu)^{1/4} K^{1/2}}{\text{Pr}_t \frac{\ln (E y_+)}{\kappa} + P_j} \qquad [A3.7]$$

where $P_j = \text{Pr}_t \frac{\pi/4}{\sin(\pi/4)} (A/\kappa)^{1/2} \left(\frac{\text{Pr}_0}{\text{Pr}_t} + 1\right) \left(\frac{\text{Pr}_t}{\text{Pr}_0}\right)^{1/4}$;
and $A = 26$.

The above equation was found to produce similar predictions to the following simple heat conduction equation but with better heat balances:

$$q_{sh} = k_{\text{eff}} \frac{\partial T}{\partial x} \qquad [A3.8]$$

ACKNOWLEDGMENTS

The authors wish to thank the steel companies: Armco, Inc. (Middletown, OH), Inland Steel Corporation (East Chicago, IN), LTV Steel (Cleveland, OH), and BHP Co. Ltd. (Wallsend, Australia) for grants which made this research possible and for the provision of data. This work is also supported by the National Science Foundation under grant No. MSS-8957195. The authors wish to recognize preliminary work on this project done by Larry Mika. Finally, thanks are due to Fluid Dynamics Inc., Evanston, IL, for help with the FIDAP program and to the National Center for Supercomputer Applications at the University of Illinois for time on the CRAY-XMP/48 and CRAY 2 supercomputers.

REFERENCES

1. H. Nakato, M. Ozawa, K. Kinoshita, Y. Habu, and T. Emi: *Trans. Iron Steel Inst. Jpn.*, 1984, vol. 24 (11), pp. 957-65.
2. K. Saito and M. Tate: *Open Hearth Furnace Proc.*, AIME, Warrendale, PA, 1973, vol. 56, pp. 238-68.
3. P. Flint: *Proc. 73rd Steelmaking Conf.*, Iron and Steel Society, Warrendale, PA, 1990.
4. A. Etienne: *Proc. 4th Int. Conf. Continuous Casting*, Stahl Eisen, Brussels, 1988, vol. 2, pp. 597-608.
5. I.D. Simpson, L.G. Moore, and C.L. Carey: *Proc. 1st European Conf. on Continuous Casting*, Associazione Italiana di Metallurgia, Florence, Italy, 1991, vol. 1, pp. 1.435-1.444.
6. S.J. Chen and T.M. Chen: *Proc. 1st European Conf. on Continuous Casting*, Associazione Italiana di Metallurgia, Florence, Italy, 1991, vol. 1, pp. 1.455-1.468.
7. K. Ayata, T. Mori, T. Fujimoto, T. Ohnishi, and I. Wakasugi: *Trans. Iron Steel Inst. Jpn.*, 1984, vol. 24 (11), pp. 931-39.
8. J. Lait, J.K. Brimacombe, and F. Weinberg: *Ironmaking and Steelmaking (Q.)*, 1974, vol. 2, pp. 90-98.
9. B. Lally, L. Biegler, and H. Henein: *Metall. Trans. B*, 1990, vol. 21B, pp. 761-70.
10. E. Upton, T.R. Satya Rao, P.H. Dauby, and R.C. Knechtges: *Iron and Steelmaker*, 1988, vol. 15 (5), pp. 51-57.
11. M. Yao, M. Ichimiya, M. Tamiya, K. Suzuki, K. Sugiyama, and R. Mesaki: *Trans. Iron Steel Inst. Jpn.*, 1984, vol. 24, p. s211.
12. T. Robertson, P. Moore, and J.F. Hawkins: *Ironmaking and Steelmaking*, 1986, vol. 13 (4), pp. 195-203.
13. N. Bessho, R. Yoda, H. Yamasaki, T. Fujii, T. Nozaki, and S. Takatori: *Proc. 6th Int. Iron and Steel Congress*, Iron and Steel Inst. Japan, Chiyoda-Ku, Tokyo, Nagoya, Japan, 1990, vol. 3, pp. 339-47.
14. B.G. Thomas and F.M. Najjar: *Appl. Mathematical Modelling*, 1991, vol. 15, pp. 226-43.
15. B.G. Thomas, L.M. Mika, and F.M. Najjar: *Metall. Trans. B*, 1990, vol. 21B, pp. 387-400.
16. D.E. Hershey: To be presented at *75th Steelmaking Conf.*, Iron and Steel Society, Toronto, ON, Canada, April 5–8, 1992.
17. R.C. Sussman, M. Burns, X. Huang, and B.G. Thomas: To be presented at *75th Steelmaking Conf.*, Toronto, ON, Canada, April 5–8, 1992.
18. M.S. Engelman: *FIDAP Theoretical Manual—Revision 4.0*, Fluid Dynamics International, Inc., Evanston, IL, 1986.
19. B.E. Launder and D.B. Spalding: *Computer Methods Appl. Mech. Eng.*, 1974, vol. 13, pp. 269-89.
20. F.M. Najjar, D.E. Hershey, and B.G. Thomas: *4th FIDAP Users Conf.*, Fluid Dynamics International, Inc., Evanston, IL, 1991, pp. 1-55.
21. C. Offerman: *Scand. J. Metall.*, 1981, vol. 10, pp. 25-28.
22. B.G. Thomas, A. Moitra, and W.R. Storkman: *Proc. 6th Int. Iron Steel Congress*, Iron and Steel Inst. Japan, Chiyoda-Ku, Tokyo, Nagoya, Japan, 1990, vol. 3, pp. 348-55.
23. X. Huang: Ph. D. Thesis, Tsinghua University, China, 1988.
24. S.V. Patankar: *Numerical Heat Transfer and Fluid Flow*, McGraw-Hill, New York, NY, 1980.
25. F. Najjar: Master's Thesis, University of Illinois, Urbana, IL, 1990.
26. S. Joo and R.I.L. Guthrie: *Proc. Int. Symp. Developments in Ladle Steelmaking and Continuous Casting*, G. Lawson, ed., Canadian Inst. Min. Metall., Montreal, PQ, Hamilton, Canada, 1990, pp. 264-89.
27. J. Lipton, W. Kurz, and W. Heinemann: *Proc. TMS Fall Meeting*, TMS, Warrendale, PA, St. Louis, MO, Oct. 24–28, 1982.
28. M. Kumada and I. Mabuchi: *Trans. Jpn. Soc. Mech. Eng.*, 1969, vol. 35, pp. 1053-61.
29. P. Sismanis and S.A. Argyropoulos: *Metall. Trans. B*, 1988, vol. 19B, pp. 859-70.
30. B.G. Thomas, F.M. Najjar, and L.J. Mika: *Proc. F. Weinberg Int. Symp. on Solidification Processing*, 29th Canadian Inst. Min. Met. Conf., J. Lait and I.V. Samarasekera, eds., Pergamon Press, Toronto, Hamilton, ON, Canada, 1990, pp. 131-45.
31. E. Hofken, H. Lax, and G. Pietzko: *4th Int. Conf. Continuous Casting*, Stahl Eisen, Brussels, Belgium, 1988, vol. 2, p. 461.
32. J. Savage and W.H. Pritchard: *J. Iron Steel Inst.*, 1954, vol. 178, pp. 269-77.